

A direct comparison of X-ray spectral models for tori in active galactic nuclei

Yuan Liu^{1*} and Xiaobo Li^{1†}

¹*Key Laboratory of Particle Astrophysics, Institute of High Energy Physics
Chinese Academy of Sciences, P.O.Box 918-3, Beijing 100049, China*

ABSTRACT

Several X-ray spectral models for tori in active galactic nuclei (AGNs) are available to constrain the properties of tori; however, the accuracy of these models has not been verified. We recently construct a code for the torus using Geant4, which can easily handle different geometries (Liu & Li 2014). Thus, we adopt the same assumptions as Murphy & Yaqoob (2009, hereafter MY09) and Brightman & Nandra (2011, hereafter BN11) and try to reproduce their spectra. As a result, we can reproduce well the reflection spectra and the strength of the Fe K α line of MY09, for both $N_{\text{H}} = 10^{24}$ and 10^{25} cm^{-2} . However, we cannot produce the strong reflection component of BN11 in the low-energy band. The origin of this component is the reflection from the visible inner wall of the torus, and it should be very weak in the edge-on directions under the geometry of BN11. Therefore, the behaviour of the reflection spectra in BN11 is not consistent with their geometry. The strength of the Fe K α line of BN11 is also different from our results and the analytical result in the optically thin case. The limitation of the spectral model will bias the parameters from X-ray spectral fitting.

Key words: radiative transfer – galaxies: active – X-rays: galaxies.

1 INTRODUCTION

Under the unification scheme of active galactic nuclei (AGNs), a toroidal structure referred as “the torus” provides anisotropic obscuration and can explain the diversity of optical and X-ray spectra of AGNs (Antonucci 1993). The torus absorbs the intrinsic X-ray spectra of AGNs (usually modelled as an absorbed power law) and also scatters the X-ray photons to produce a Compton hump at ~ 20 keV. The abundant and high quality data from recent X-ray satellites enable us to investigate the X-ray properties of AGNs in unprecedented detail. The structure of the tori in AGNs can be constrained if an X-ray spectral model of the tori is specified. Compared with the models for the disk geometry, e.g. `pexrav` and `pexmon` (Magdziarz & Zdziarski 1995; Nandra et al. 2007), several more physical and realistic models have been recently constructed to model the X-ray spectrum from the torus, which adopt a toroidal structure and self-consistently include fluorescent lines (Ikeda et al 2009, hereafter IK09; Murphy & Yaqoob 2009, hereafter MY09; Brightman & Nandra 2011, hereafter BN11). These models have been applied to individual AGNs to derive the covering factor and column density of the

sources (Singh et al. 2012; Yaqoob 2012; Arévalo et al. 2014; Gandhi et al. 2014). With a survey sample, these models are helpful for finding Compton thick AGNs and determining how the tori evolve with the properties of AGNs, such as the correlation between the covering factor and luminosity (Brightman & Nandra 2012; Brightman & Ueda 2012; Brightman et al. 2014; Buchner et al. 2014; Ricci et al. 2014). In spite of the success of the application of such models, the accuracy and validity of such models have not been independently verified. The parameters from these models will be biased if there are some limitations or errors in these models. We recently constructed an X-ray spectral model for the tori in AGNs using Geant4, which can handle the smooth and clumpy tori by the same code. Thus, if we adopt the same assumptions used by MY09, BN11 and IK09 (e.g. geometries, cross sections and element abundances), our Geant4 code should reproduce their result, in principle. In Section 2, we present the quantitative comparison with the public models in MY09 and BN11. Because the results of IK09 are not public, we just use the general trend presented in IK09 as a reference. In Section 3, we discuss the difference found in the comparison, and we show our main conclusions in Section 4.

* E-mail: liuyuan@ihep.ac.cn

† E-mail: lixb@ihep.ac.cn

2 SIMULATIONS FOR COMPARISON

The details of our simulation method are presented in Liu & Li (2014). We have included several physical processes in our code, e.g. photoelectric effect, Compton scattering, Rayleigh scattering, γ conversion, fluorescent lines and Auger process. Similar physical processes have been considered in the simulations of MY09 and BN11. Thus, it is convenient to modify our code to simulate their cases. Our code and the simulations by MY09 and BN11 have included multi-scatterings, e.g. Figure 7 in Liu & Li (2014). We then use the same assumptions adopted by BN11 and MY09 respectively to try to reproduce their results¹. The incident flux is 5×10^8 photons (1-500 keV) for all simulations presented in this paper.

2.1 Results under the assumptions of MY09

The geometry of MY09 is shown in Figure 1. The half-opening angle of the torus is 60° .

Using the same geometry, cross sections, element abundances and incident spectra (a single power law with the photon index $\Gamma = 1.8$), we can well reproduce MY09's continua, for both $N_H = 10^{24}$ and 10^{25} cm^{-2} (Figure 2, where θ_{in} is the inclination angle relative to an observer). The direct component is not shown for clarity. Since the shape of the scattered component is determined by both the scattering and absorption processes (e.g. Fe K absorption edge at 7 keV), these results verify the accuracy of MY09's simulations.

We have further compared the equivalent width (EW) of the Fe K α line of our simulations with that in Figure 8 of Murphy & Yaqoob (2011), which is the erratum of MY09. The photon index Γ is 1.9 in these simulations. For $N_H = 10^{24}$ and 10^{25} cm^{-2} , the difference of EWs between our simulations and MY09's model is smaller than 1% for most of the directions. The maximum deviation is $\sim 2\%$ for $N_H = 10^{24} \text{ cm}^{-2}$ and $\cos \theta_{\text{in}} = 0.3 - 0.4$. This small deviation could be due to the different simulation method adopted by MY09. The accuracy of this model is sufficient, since the statistical error of EW(Fe K α) in observed X-ray spectra is larger than 10% in most cases (Liu & Wang 2010; Shu, Yaqoob, & Wang 2011).

2.2 Results under the assumptions of BN11

The geometry of BN11 is shown in Figure 3. The half-opening angle of the torus is fixed at 60° .

The inner radius of the torus is assumed to be zero in BN11's model. The comparison between the BN11's model and our results is shown in Figure 4 ($\Gamma=1.8$). The total spectra are shown, i.e. direct+ scattered components, since BN11's model only provides the total spectra. The fluorescent lines (including the Compton shoulders) in the spectra of our simulations are not shown for clarity, because it is not easy to directly compare the strength of such a quasi- δ function in the figure.

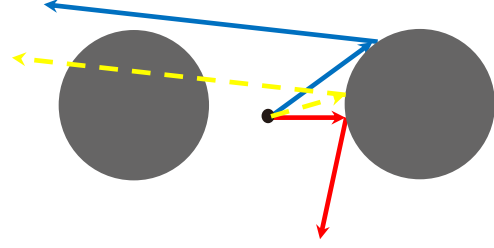


Figure 1. Geometry of MY09. The red and blue arrows indicate the possible trajectories of low-energy scattered photons that can escape to face-on and edge-on directions, respectively. The yellow arrows indicate the trajectories of low-energy scattered photons that will be absorbed by the near side of the torus for edge-on directions.

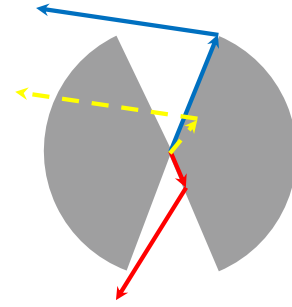


Figure 3. Geometry of BN11. The red and blue arrows indicate the possible trajectories of low-energy scattered photons that can escape to face-on and edge-on directions, respectively. The yellow arrows indicate the trajectories of low-energy scattered photons that will be absorbed by the near side of the torus for edge-on directions.

Although the continua of the face-on directions are consistent with each other, the spectra of the edge-on directions, especially for low-energy band, are significantly different. It seems there is an “additional” component at the low-energy band in the simulations of BN11.

We have further compared EW(Fe K α) of our simulations with that in Figure 3 of BN11. The photon index Γ is 2.0 in these simulations. For the face-on direction ($\theta_{\text{tor}} = 60^\circ$ and $\theta_{\text{in}} = 0 - 37^\circ$), EW(Fe K α) of BN11 is lower than our simulation results by 30% and 35% for $N_H = 10^{24}$ and 10^{25} cm^{-2} , respectively. For the edge-on direction ($\theta_{\text{tor}} = 60^\circ$ and $\theta_{\text{in}} = 78 - 90^\circ$), their EW(Fe K α) is higher than our results by 60% for $N_H = 10^{24} \text{ cm}^{-2}$. Due to the large deviation of the continuum of the edge-on direction for $N_H = 10^{25} \text{ cm}^{-2}$, we have not compared the EW(Fe K α) in this case.

We explore these discrepancies in detail in the next section.

3 DISCUSSION

Under the N_H discussed in Figure 2 and 4, the direct component is highly absorbed in the low-energy band. Thus, the low-energy spectra are dominated by the reflection from the visible inner wall of the torus for a given inclination angle, which is referred to as the ‘reflection component 2’ in IK09 (the Figure 2 in IK09 illustrates its geometry and origin).

¹ The model file of MY09 is downloaded from <http://mytorus.com/model-files-mytorus-downloads.html>. The model file of BN11 is downloaded from <http://www.mpe.mpg.de/~mbright/data/torus1006.fits>

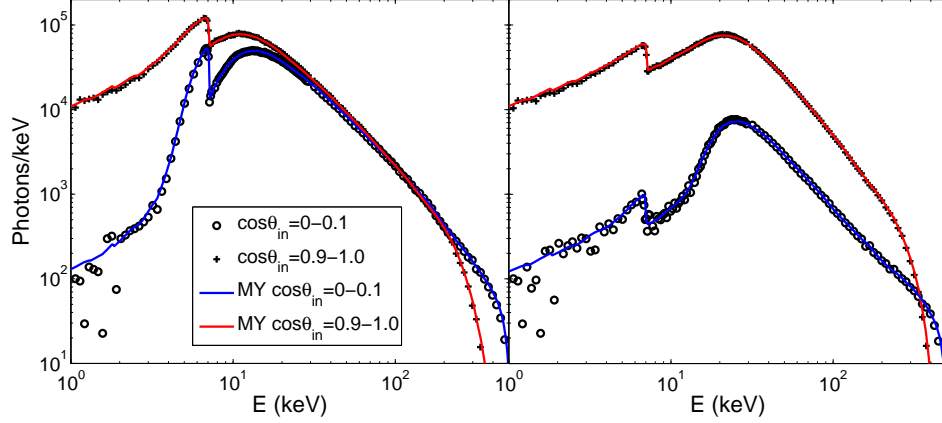


Figure 2. Spectra under MY09’s assumptions with $N_{\text{H}} = 10^{24}$ (left) and 10^{25} cm^{-2} (right). Only scattered continua are shown for clarity. The scattered fluorescent photons are treated as the portion of emission lines and not shown here.

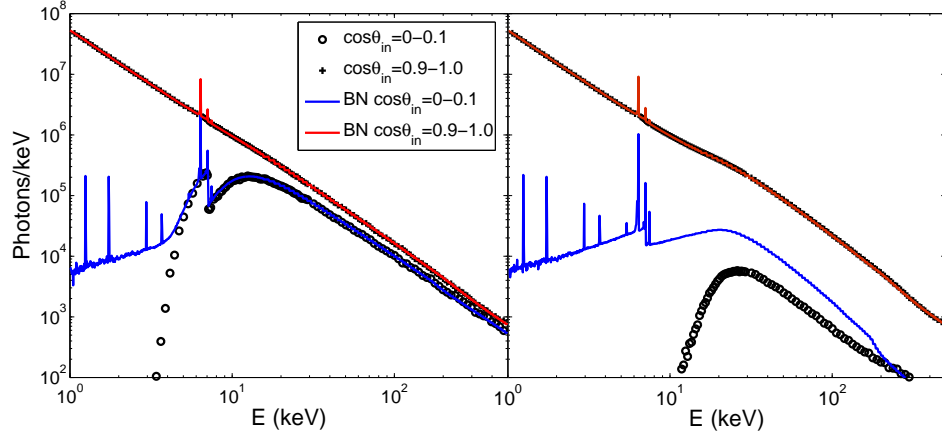


Figure 4. Spectra under BN11’s assumptions with $N_{\text{H}} = 10^{24}$ (left) and 10^{25} cm^{-2} (right). The total spectra (scattered+direct) are shown, but the fluorescent lines (including the Compton shoulders) in our simulation are not shown for clarity. The half-opening angle is assumed to be 60° .

The strength of this component depends on the geometry of the torus, i.e. the location and shape of the surface, and should also depend on the inclination angles. Therefore, to judge whether the results of BN11’s model in Figure 4 are reasonable, we investigate the variation of this component with inclination angles in different models.

Because $r_{\text{in}}/r_{\text{out}} = 0.01$ adopted in the simulations of IK09 is small, IK09’s geometry is actually very similar to that of BN11, i.e. the N_{H} distribution is almost constant for different inclination angles. We plot the distribution of N_{H} using equation (3) in IK09 to show this (Figure 5).

As shown in the Figure 9 in IK09, the ‘reflection component 2’ significantly decreases with increasing inclination angles, i.e. it is very weak in the edge-on directions.

A similar trend is also observed in MY09’s model (Fig-

ure 6), though the variation is not as dramatic as that in the Figure 9 in IK09. We will explain this later. The spectrum at 1 keV with inclination angle $\theta_{\text{in}} = 65^\circ$ is higher than that with $\theta_{\text{in}} = 85^\circ$ by more than one order.

However, the strength of this low-energy reflection component in BN11’s model only weakly depends on the inclination angles (Figure 7). The spectrum at 1 keV with $\theta_{\text{in}} = 65^\circ$ is only higher than that with $\theta_{\text{in}} = 85^\circ$ by a factor of two.

The strength of this low-energy component depends on the visibility of the inner wall of the torus at different inclination angles. Under the geometry of MY09, since the central part of the torus is empty, the whole inner surface of the torus is directly illuminated by the central source. As a result, a considerable part of the inner wall is visible when the inclination angle is slightly larger than the half-opening

angle of the torus (the blue arrows in Figure 1); even for the edge-on case, the rim of the inner wall is still visible but the majority of reflection in low-energy band is absorbed by the near side of the torus (the blue and yellow arrows in Figure 1). This can explain the trend observed in Figure 6.

To further support the above explanation, in Figure 8 we also plot the positions of the scatterings of the observed photons in 1-2 keV, i.e. the photons have experienced scatterings and finally escaped to the observer. The distributions of the positions of the scatterings for two directions are shown. The scatterings of low-energy photons can only occur at the skin of the torus; otherwise, they will be absorbed in the body of the torus. As the inclination angle moves to the edge-on direction, the visible part also moves to the rim. If the scattered photons intend to escape from the edge-on direction, the scatterings should occur at the rim of the torus; otherwise, they will be absorbed by the near side of the torus.

For the BN11 geometry, the torus extends to the centre and the column densities are the same for different inclination angles. As a result, if the low-energy photons are scattered and can escape to the observer, they can only be scattered very near to the centre; otherwise, they will be absorbed before reaching a large radius. Therefore, the reflection component is only visible when the inclination is slightly larger than the half-opening angle (a few degrees). The possible trajectory of the scattered photons is indicated by the arrows in Figure 3. For the edge-on case, the scattered region is obscured by the near side of the torus. If the scattered photons intend to escape to the edge-on direction, they should be scattered at a large radius and follow the way indicated by the blue arrows in Figure 3. However, such photons should be rare, since most of them will be absorbed before reaching the large radius. This is also the reason for the significant decrease found in the Figure 9 in IK09. We plot the positions of the scatterings in Figure 9, which are indeed concentrated in the central part of the torus. The region is very small compared with the outer radius (2 pc) of the torus. Therefore, this reflection component in the edge-on direction should be very weak under the geometry of BN11 and IK09, as shown by our simulations in Figure 4.

As mentioned in Section 2.2, the $\text{EW}(\text{Fe K}\alpha)$ of BN11 is also different from our simulations. For optically thin case, $\text{EW}(\text{Fe K}\alpha)$ can be analytically calculated, e.g. by equation (5) in MY09, and nearly isotropic. Thus, we take this analytical result as the benchmark test of BN11's model and our simulations. Under the assumption in Figure 3 of BN11, the analytical $\text{EW}(\text{Fe K}\alpha)$ is 3.7 eV for $\Gamma = 2.0$, $\theta_{\text{tor}} = 60^\circ$, and $N_{\text{H}} = 10^{22} \text{ cm}^{-2}$. The $\text{EW}(\text{Fe K}\alpha)$ of our simulation under the same assumption is well consistent with 3.7 eV (at better than 1% level). However, the EW of BN11's model is about 4.4 eV for the same case. Since their continua at 6.4 keV are consistent with our results at 1% level even for the edge-on case of $N_{\text{H}} = 10^{24} \text{ cm}^{-2}$, there should be some problems in the transportation of Fe K α photons, which might be related to the problem inducing the overestimate of the reflection component.

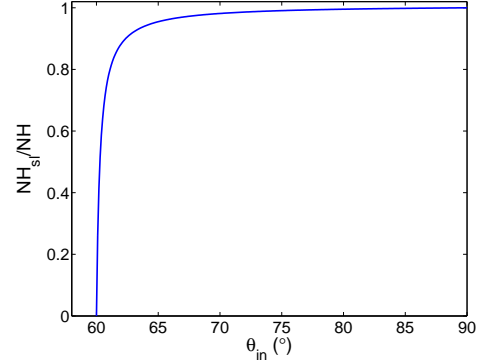


Figure 5. Ratio between the column density along the line of sight and the maximum N_{H} in IK09 (half-opening angle= 60° and $r_{\text{in}}/r_{\text{out}} = 0.01$). It is almost constant except for the angles near the edge of the torus.

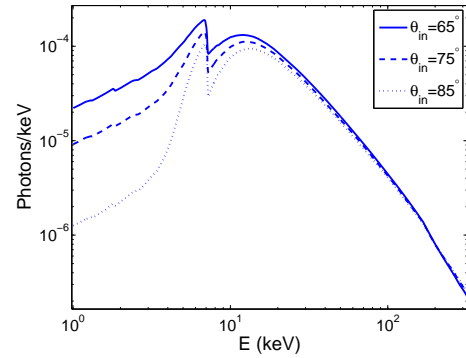


Figure 6. The scattered component is significantly suppressed in the edge-on direction under MY09's geometry.

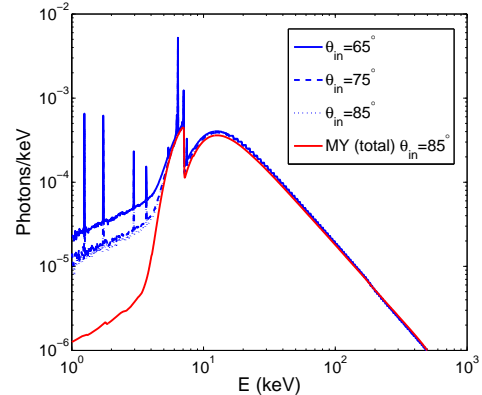


Figure 7. The scattered component only weakly depends on the inclination angles in BN11's model. The strength of the low-energy component in edge-on direction is much higher than that produced by MY09's model (scattered and direction components are added).

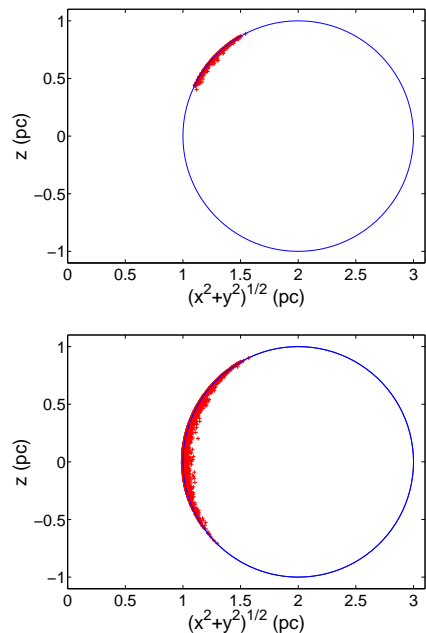


Figure 8. Positions of the scatterings of the photons (1–2 keV) escaped to $\cos \theta_{\text{in}} = 0–0.2$ (top) and $\cos \theta_{\text{in}} = 0.4–0.5$ (bottom) under MY09's geometry. The 3-D positions are projected onto a plane to show the distribution more clearly. The blue line shows the boundary of the torus and the central X-ray source is located at the origin.

4 CONCLUSIONS

With the code constructed using Geant4, we can reproduce well the continua and the strength of Fe $K\alpha$ line of MY09's model. However, the reflection component in the low-energy band is much lower than that of BN11's model. We have discussed the origin of this reflection component and shown that the scattered region is concentrated in the centre and invisible in the edge-on directions under the BN11's geometry. Therefore, it seems the strength of the reflection component is overestimated in BN11 for the edge-on directions. The strength of Fe $K\alpha$ line of BN11's model is also different from our results and the analytical result in the optically thin case, which is likely to be due to the problem in the transportation of Fe $K\alpha$ photons. The accuracy of the model is crucial to any conclusions from the spectral fitting.

ACKNOWLEDGMENTS

This work is supported by the National Natural Science Foundation of China under grant Nos. 11103019, 11303027, 11133002, and 11103022.

REFERENCES

- Antonucci R., 1993, ARA&A, 31, 473
- Arévalo P., et al., 2014, ApJ, 791, 81
- Brightman M., Nandra K., 2012, MNRAS, 422, 1166
- Brightman M., Nandra K., 2011, MNRAS, 413, 1206
- Brightman M., Nandra K., Salvato M., Hsu L.-T., Aird J., Rangel C., 2014, MNRAS, 443, 1999

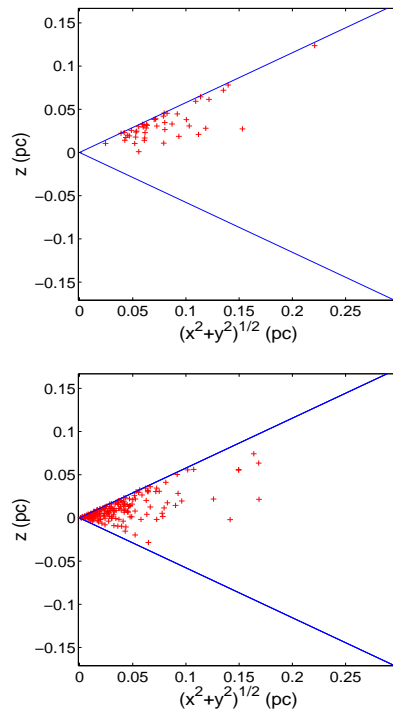


Figure 9. Positions of the scatterings of the photons (1–2 keV) escaped to $\cos \theta_{\text{in}} = 0–0.49$ (top) and $\cos \theta_{\text{in}} = 0.49–0.5$ (bottom) under BN11's geometry. The intervals of $\cos \theta_{\text{in}}$ are different from that in Figure 8, since the number of the scattered photons under BN's geometry rapidly decreases when the inclination angle is larger than the half-opening angle of the torus by a few degrees. The 3-D positions are projected onto a plane to show the distribution more clearly. The inner radius of the torus is 0 pc and the outer radius is 2 pc (not shown). The blue line shows the boundary of the torus and the central X-ray source is located at the origin.

- Brightman M., Ueda Y., 2012, MNRAS, 423, 702
- Buchner J., et al., 2014, A&A, 564, A125
- Gandhi P., et al., 2014, arXiv:1407.1844
- Ikeda S., Awaki H., Terashima Y., 2009, ApJ, 692, 608
- Liu T., Wang J.-X., 2010, ApJ, 725, 2381
- Liu Y., Li X., 2014, ApJ, 787, 52
- Magdziarz P., Zdziarski A. A., 1995, MNRAS, 273, 837
- Murphy K. D., Yaqoob T., 2009, MNRAS, 397, 1549
- Murphy K. D., Yaqoob T., 2011, MNRAS, 415, 3962
- Nandra K., O'Neill P. M., George I. M., Reeves J. N., 2007, MNRAS, 382, 194
- Ricci C., Ueda Y., Ichikawa K., Paltani S., Boissay R., Gandhi P., Stalevski M., Awaki H., 2014, A&A, 567, A142
- Shu X. W., Yaqoob T., Wang J. X., 2011, ApJ, 738, 147
- Singh V., Risaliti G., Baito V., Shastri P., 2012, MNRAS, 419, 2089
- Yaqoob T., 2012, MNRAS, 423, 3360

This paper has been typeset from a \LaTeX file prepared by the author.